ELSEVIER

Contents lists available at ScienceDirect

Materials Letters

journal homepage: www.elsevier.com/locate/matlet



Cracks-free yet ultrafine-grained 7050 aluminium alloys by selective laser melting

Xuyang Huang ^a, Qi Zhu ^{a,*}, Lv Liu ^b, Yu Liu ^a, Yue Cui ^a, Qiong Wu ^a, Nailin Tang ^a, Dong Yin ^a, Zhifeng Liu ^a, Xiaochuan Jiang ^a, Xin Gong ^a, Jiahui Du ^c

- ^a Central Hospital Affiliated to Shenyang Medical College, Shenyang 110032, China
- ^b Benxi Central Hospital, Benxi City 117000, China
- ^c Northeastern University, Shenyang 110819, China

ARTICLE INFO

Keywords: Aluminium alloy Selective laser melting Cracks-free Equiaxed grains Strength-ductility synergy

ABSTRACT

Eliminating hot cracking and achieving a good strength-ductility synergy in selective laser melted (SLMed) high-strength aluminium alloys remain challenging. We here inoculated 7050 high-strength aluminium alloy with 2 wt% Ti nanoparticles to eliminate hot cracking during SLM. Furthermore, ultrafine equiaxed grains with random textures were achieved in SLMed 7050 – 2 wt% Ti alloy, in contrast to the textured columnar grains observed in SLMed 7050 alloy. A high tensile yield strength of 393 MPa and an elongation of 11.6 % were achieved in SLMed 7050 – 2 wt% Ti alloy.

1. Introduction

Aluminium alloys have been widely used not only for aerospace and automotive applications, but also for medical applications (e.g., orthopedic, endoscopic, spinal, trauma, and surgical scenarios), due to their low density, high specific yield strength, and reasonable tensile ductility, etc. [1]. As a typical additive manufacturing (AM) technology, selective laser melting (SLM) enables to rapidly fabricate complex-geometry components layer-upon-layer [2]. Although some commercial alloys with exceptional mechanical properties have been successfully fabricated via SLM [3,4], commercial aluminium alloys often encounter severe hot tearing during SLM [2], except a few near-eutectic Al-Si alloy with a narrow solidification range [5]. Such severe hot tearing often occurs along the grain boundaries of textured columnar grains that are triggered by steep temperature gradients intrinsic to SLM. How to process these high-strength aluminium alloys via SLM remains a long-standing challenge.

Recently, it has been proven that incorporating inoculants can promote the heterogenous nucleation and the formation of equiaxed grains, which easily accommodate strains and suppress hot cracking during SLM. However, most inoculants (e.g. Nb, Ta, Sc) are source-critical, costly, and/or heavy, the minor addition of which would increase the density and the cost of the AM aluminium alloys. On the other hand, although some lightweight and/or cheap grain refiners were tried, the

resultant tensile properties, especially the tensile ductility, are limited [6]. Herein, we selected Ti nanoparticles as an inoculant for 7050 aluminium alloys during SLM. Among vast inoculants, Ti is relatively lightweight and cheap, and has been proven effective for non-weldable aluminium alloys, such as 2xxx series aluminium alloys. The resultant alloy in the current study shows good printability and a good strength-ductility combination.

2. Experimental

The detailed information regarding the powder preparation, SLM processing, microstructural and mechanical characterization have been given in Supplementary File.

3. Results and discussion

Fig. 1 presents typical micrographs of the 7050 aluminium alloy particles inoculated with 2 wt% Ti elemental particles. Obviously, the 7050 aluminium alloy particles are nearly spherical in shape with an average diameter of approx. 30 μ m (Fig. 1a). Occasionally, gas pores were observed within the 7050 particles (Fig. 1a). The nanoscale Ti elemental particles are uniformly distributed on the micro-sized 7050 aluminium alloy particle surface, with no obvious agglomeration (Fig. 1b). This also demonstrates that our powder mixing approach is

E-mail address: Emergency_zhuqi@163.com (Q. Zhu).

^{*} Corresponding author.

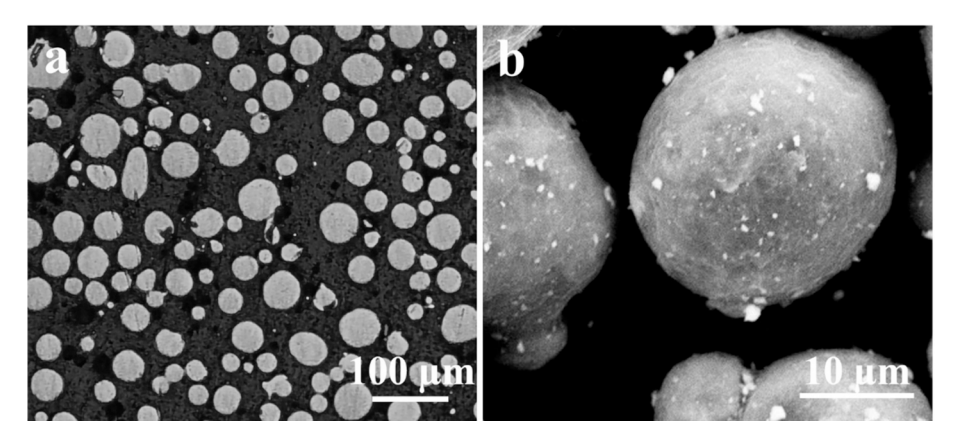


Fig. 1. A. A typical optical microscopy (OM) micrograph showing the near-spherical shape of the 7050 aluminium alloy particles, with occasional gas pores. b. A scanning electron microscopy (SEM) micrograph of the composite powder particle showing the uniform distribution of the nanoscale Ti elemental particles on the micro-sized 7050 aluminum alloy particles.

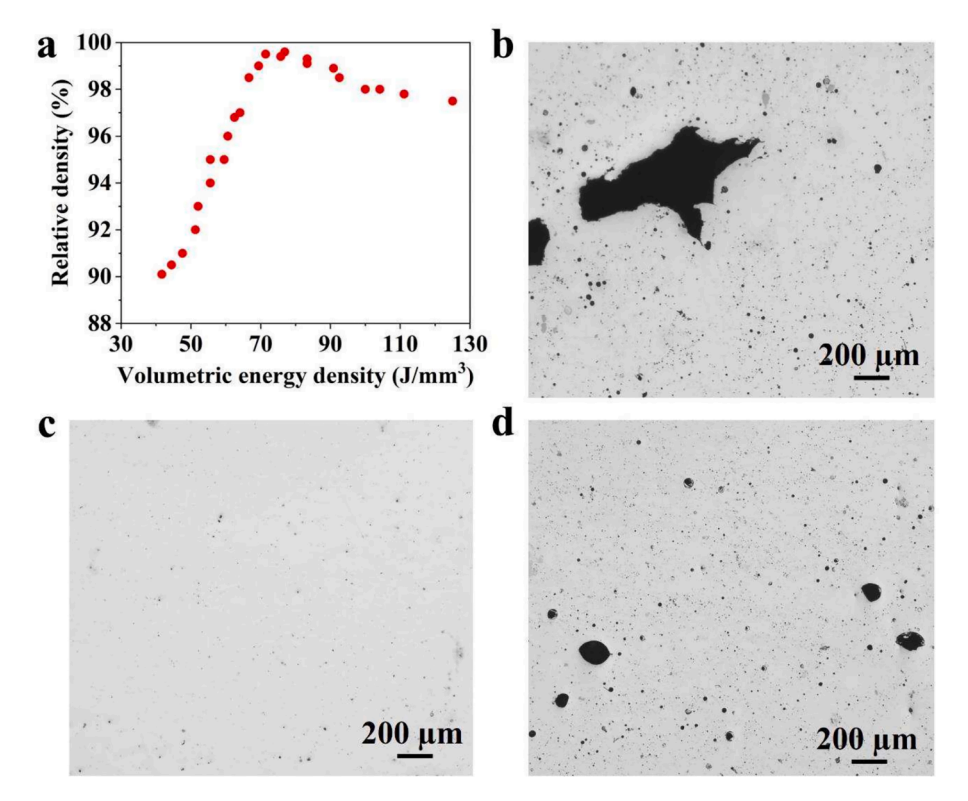


Fig. 2. A. Relative density plot as a function of the volumetric energy density. b-d. Typical OM micrographs of the SLMed 7050 – 2 wt% Ti alloy built with 55, 76, and 92 J/mm³.

effective to uniformly mix micro-sized particles together with nanoscale ones.

Fig. 2a presents the relative density of the SLMed 7050-2 wt% Ti alloy built with different laser powers and laser scan speeds which lead to a wide range of the volumetric energy density. Clearly, the relative density value increases with the increase in the volumetric energy density, and peaks at approx. 76 J/mm^3 followed by a slight decrease. Fig. 2b-d present typical OM micrographs of the SLMed 7050-2 wt% Ti alloy built with low, medium, and high regimes of the volumetric energy density, respectively. It can be seen that the low relative density at a volumetric energy density of 55 J/mm^3 can be attributed to the formation of large-sized lack-of-fusion defects (Fig. 2b). Lack-of-fusion pores are often formed due to the insufficient heat input, such as low laser powers, or high laser scan speeds. Insufficient heat input usually leads to the insufficient overall rheological properties within the melt

pool and hence very poor metallurgical bonding between particles [7]. The highest relative density was achieved at a laser power of 250 W and a laser scan speed of 1100 mm/s, resulting in a volumetric energy density of 76 J/mm³. Consistent with the relative density plot shown in Fig. 2a, the OM micrograph of the sample built with 76 J/mm³ demonstrates a very dense microstructure, with few pores observed (Fig. 2c). Too high heat input triggers the formation of numerous spherical pores (Fig. 2d), indicative of the key-holing mode activated [8]. Specifically speaking, when the energy input is superhigh, the material vaporization would be more frequent, and the recoil pressure would be generated towards the melt pool. Therefore, the liquid is pressed downwards to the melt pool bottom, leading to the formation of deeper and narrower melt pools. Such melt pools are very unstable and the collapse of the liquid would generate a vapor void in the melt pool. So we can see that numerous spherical keyhole pores are formed after the peak at 76 J/

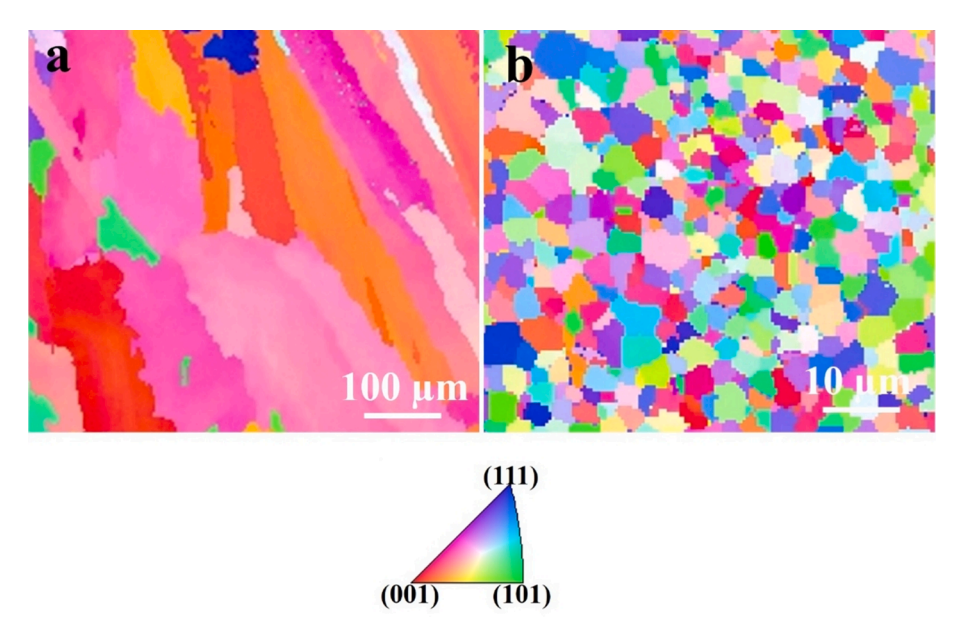


Fig. 3. A, b. EBSD IPF maps of the SLMed 7050 aluminium alloy and the SLMed 7050 - 2 wt% Ti alloy, respectively.

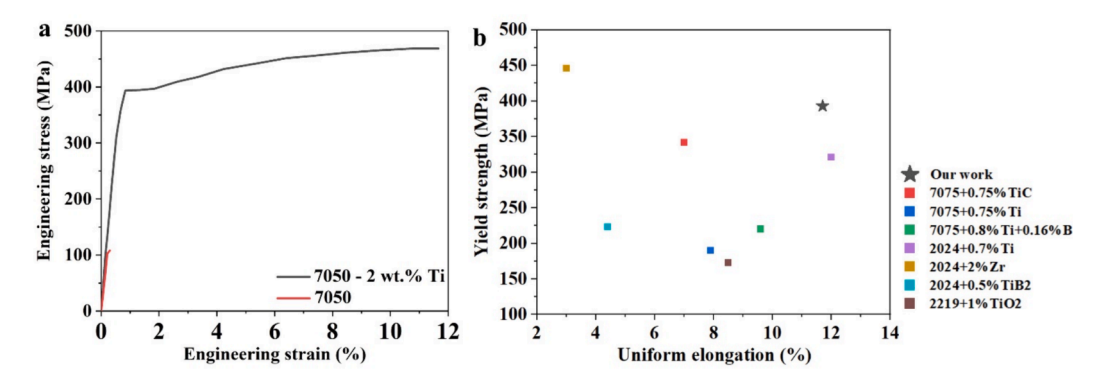


Fig. 4. A. Engineering tensile stress–strain curves of the SLMed 7050 aluminium alloy and the SLMed 7050 – 2 wt% Ti alloy. b. A map of yield strength vs. uniform elongation of our alloy as compared with some typical as-printed non-weldable aluminium alloys via additive manufacturing. The tensile properties are acquired from Refs. [10–15].

mm³, resulting in the relative density decrease. It should be noted that the process optimization was performed under a constant layer thickness of 30 μm and a constant hatch spacing of 100 μm . The variation of the layer thickness and hatch spacing would definitely affect the optimal laser power-laser scan speed combination. Often, the increase in the layer thickness and hatch spacing would require an increased energy input to ensure good bonding between adjacent layers and between adjacent tracks. At last, we noticed that no cracks were observed in these SLMed 7050 – 2 wt% Ti alloy samples.

Fig. 3a-b present the electron backscattered diffraction (EBSD) inverse pole figure (IPF) maps of the SLMed 7050 aluminium alloy and the 7050 – 2 wt% Ti alloy, respectively. The observed planes for both maps are the XZ-plane, with the X-, and Z-axis aligned horizontally and vertically, respectively. It can be seen that the SLMed 7050 aluminium alloy possesses typical coarse columnar grained structures (Fig. 3a). These columnar grains grow along the Z axis (or the build direction), aligning their $\langle 1\,0\,0\rangle$ crystallographic orientations parallel to the build direction. The width of these columnar grains was estimated to be approx. $20-150~\mu m$. In contrast, a totally distinct microstructure was observed in the SLMed 7050 – 2 wt% Ti alloy, as shown in Fig. 3b. The SLMed 7050 – 2 wt% Ti alloy exhibits ultrafine equiaxed grains of approx. $1-5~\mu m$ in average grain size. Furthermore, the random colors in the EBSD IPF map (Fig. 3b) also confirms the development of rather

random textures. The elimination of the highly textured columnar grains in the presence of the nanoscale Ti particles can be attributed to the following reasons. Those Ti nanoparticles would in situ react with Al in the melt pool, triggering the formation of a high density of Al $_3$ Ti nanoparticles. From a crystallographic point of view, Al $_3$ Ti nanoparticles are effective heterogeneous nucleating substrates for primary Al [9], and hence would promote the formation of profuse equiaxed crystals in the solidification front, which prohibit the growth of columnar grains, if any. As such, a fully equiaxed grained microstructure with random crystallographic textures has been achieved in the SLMed 7050 – 2 wt% Ti alloy.

Fig. 4a presents the engineering tensile stress–strain curves of the SLMed 7050 aluminium alloy and the SLMed 7050 – 2 wt% Ti alloy. Without the introduction of the Ti particles, the SLMed 7050 aluminium alloy fails prematurely, with an unacceptable strength and ductility. The premature failure can be attributed to the bad printability-induced preexisting cracks. In contrast, the incorporation of Ti nanoparticles significantly improves the tensile properties. Specifically, the SLMed 7050 – 2 wt% Ti alloy exhibits a yield strength of 393 MPa, an ultimate tensile strength of 468 MPa, and a tensile ductility of 11.6 %. On the one hand, the improved tensile properties benefit from the elimination of intergranular hot cracks that easily trigger premature failure. On the other hand, the formation of ultrafine equiaxed grains can strengthen

and ductilize the materials simultaneously owing to the well-known grain refinement strengthening mechanism. Fig. 4b presents a map of tensile yield strength vs. uniform elongation of our alloy as compared to typical non-weldable aluminium alloys via additive manufacturing, showing the good tensile properties of our SLMed 7050 – 2 wt% Ti alloy.

4. Conclusions

In this work, 7050-2 wt% Ti samples were successfully fabricated by SLM. A systematic process optimization was performed to minimize lack-of-fusion and key-hole defects. The incorporation of Ti elemental nanoparticles suppresses the hot cracking and promotes the formation of ultrafine equiaxed grains, with random crystallographic textures. As such, a high yield strength of 393 MPa and a good elongation of 11.6 % have been achieved.

CRediT authorship contribution statement

Xuyang Huang: Conceptualization, Data curation, Methodology, Writing – original draft, Writing – review & editing. Qi Zhu: Conceptualization, Funding acquisition, Writing – review & editing. Lv Liu: Formal analysis. Yu Liu: Formal analysis. Yue Cui: Formal analysis. Qiong Wu: Formal analysis. Nailin Tang: Formal analysis. Dong Yin: Formal analysis. Zhifeng Liu: Formal analysis. Xiaochuan Jiang: Formal analysis. Xin Gong: Formal analysis. Jiahui Du: Formal analysis.

Declaration of competing interest

The authors declare that they have no known competing financial interests or personal relationships that could have appeared to influence the work reported in this paper.

Data availability

Data will be made available on request.

Acknowledgement

The authors acknowledge the financial support from the Liaoning Provincial Department of Education Basic Science Research Project (No. LJKZ1154) and Middle-aged and Youth Science and Technology Innovative Talents of Shenyang City (No. CR210437).

Appendix A. Supplementary data

Supplementary data to this article can be found online at $\frac{https:}{doi.}$ org/10.1016/j.matlet.2024.136804.

References

- [1] T. Dursun, C. Soutis, Mater. Des. 1980-2015 (56) (2014) 862-871.
- [2] P.A. Rometsch, Y. Zhu, X. Wu, A. Huang, Mater. Des. 219 (2022) 110779.
- [3] Y.M. Wang, T. Voisin, J.T. McKeown, J. Ye, N.P. Calta, Z. Li, Z. Zeng, Y. Zhang, W. Chen, T.T. Roehling, R.T. Ott, M.K. Santala, P.J. Depond, M.J. Matthews, A. V. Hamza, T. Zhu, Nat. Mater. 17 (2018) 63–71.
- [4] Z. Song, W. Gao, D. Wang, Z. Wu, M. Yan, L. Huang, X. Zhang, Materials 14 (2021) 1001.
- [5] L. Thijs, K. Kempen, J.-P. Kruth, J. Van Humbeeck, Acta Mater. 61 (2013) 1809–1819.
- [6] J.H. Martin, B.D. Yahata, J.M. Hundley, J.A. Mayer, T.A. Schaedler, T.M. Pollock, Nature 549 (2017) 365–369.
- [7] T. Mukherjee, T. DebRoy, J. Manuf. Process. 36 (2018) 442-449.
- [8] L. Johnson, M. Mahmoudi, B. Zhang, R. Seede, X. Huang, J.T. Maier, H.J. Maier, I. Karaman, A. Elwany, R. Arróyave, Acta Mater. 176 (2019) 199–210.
- [9] M.-X. Zhang, P.M. Kelly, M.A. Easton, J.A. Taylor, Acta Mater. 53 (2005) 1427–1438.
- [10] T. Zheng, S. Pan, N. Murali, B. Li, X. Li, Mater. Lett. 319 (2022) 132268.
- [11] Q. Tan, Z. Fan, X. Tang, Y. Yin, G. Li, D. Huang, J. Zhang, Y. Liu, F. Wang, T. Wu, X. Yang, H. Huang, Q. Zhu, M.-X. Zhang, Mater. Sci. Eng. A 821 (2021) 141638.
- [12] B. Huang, Y. Liu, Z. Zhou, W. Cheng, X. Liu, Vacuum 200 (2022) 111030.
- [13] Q. Tan, J. Zhang, Q. Sun, Z. Fan, G. Li, Y. Yin, Y. Liu, M.-X. Zhang, Acta Mater. 196 (2020) 1–16.
- [14] B. Chen, X. Xi, T. Gu, C. Tan, X. Song, J. Mater. Res. Technol. 9 (2020) 14223–14236.
- [15] G. Li, Y. Huang, X. Li, C. Guo, Q. Zhu, J. Lu, Addit. Manuf. 60 (2022) 103296.